

Strong driving of a single coherent spin by a proximal chiral ferromagnetM. S. Wolf,¹ R. Badea,¹ M. Tader,² and J. Berezovsky^{1,*}¹*Department of Physics, Case Western Reserve University, Cleveland, Ohio 44106, USA*²*Department of Physics, Cornell University, Ithaca, New York 14853, USA*

(Received 19 January 2017; revised manuscript received 8 May 2017; published 18 July 2017)

We experimentally investigate the influence of a driven, dynamic vortex magnetization state on an individual nitrogen-vacancy (NV) spin in diamond. The vortex core can be translated within the ferromagnet using an applied magnetic field, allowing us to map out the spatial dependence of the interaction. The vortex displacement is determined using magneto-optical microscopy, while the vortex's influence on the spin is probed using optically detected magnetic resonance to measure the Rabi oscillation frequency between spin levels. We find that the close proximity of the vortex core to the NV (within about 200 nm) leads to more than an order of magnitude enhancement of the Rabi frequency. The NV/vortex interaction differs significantly for transitions to the $m_s = +1$ and $m_s = -1$ spin states, which we attribute to the chiral nature of the vortex state dynamics. We compare the results with micromagnetic simulations and a simple analytical model to shed light on the mechanisms behind the observed effects.

DOI: [10.1103/PhysRevB.96.014424](https://doi.org/10.1103/PhysRevB.96.014424)

The interactions between single coherent spin systems and proximal ferromagnetic (FM) structures have led to greater understanding of the physics of the single spin and FM systems themselves [1], as well as opening pathways towards applications in which FM elements tailor the magnetic environment of one or more spin qubits [2–4]. In recent years, the spin of a nitrogen-vacancy (NV) center in diamond has emerged as a key platform for probing these interactions due to their atomic-scale size, convenient optical spin initialization and readout, and robust spin coherence in ambient conditions [5–7]. NVs coupled to microscale or nanoscale FM structures have been proposed for applications ranging from spin addressability [8], to enhanced spin sensing [9,10], to spin-wave-mediated coupling between spins [11]. Much experimental work to date has focused on the effect of the static FM fringe field on the evolution of the NV spin. Recent work, however, has indicated that the magnetization dynamics of a FM element lead to nontrivial effects on a proximal NV spin [12–14]. This paper explores these dynamic phenomena, which may enable or limit future applications.

Here, we probe the influence of a dynamic FM vortex state on proximal individual NV spins. The spin texture of a vortex state displays a range of properties that make it a useful model system for studying spin/FM interactions in general. These properties include a strong magnetic fringe field (and large field gradient) produced by the vortex core [8], and a discrete spectrum of localized modes spanning a frequency range from hundreds of MHz to GHz. Moreover, the vortex core can be scanned within the FM using an in-plane magnetic field, permitting tuning of the spin/FM interactions. The position of the vortex core can be controlled with nanoscale precision, on timescales of tens of nanoseconds [15]. We use this capability to scan the vortex core along a path, while monitoring the effect on a proximal NV spin. We find that, when driving NV spin transitions with an applied microwave (MW) field, the proximity of the vortex results in modification of both the

spin resonance linewidth Γ and the coherent Rabi transition rate Ω between spin states. Both the increase of Γ and Ω are attributed to the coherent influence of the vortex, so Γ can be used as a relaxometric probe of Ω . We first demonstrate this effect by scanning the vortex core along a line, approaching the NVs. We then scan the vortex along different paths to map out the effect of the vortex on the spin dynamics. When the vortex/spin coupling is strongest, we find that Ω is enhanced by more than an order of magnitude. Further, we find that the chirality of the vortex dynamics leaves an imprint on this effect, resulting in different Ω_+ and Ω_- for transitions to the spin states with $m_s = +1$ and $m_s = -1$. Comparison of these results to both micromagnetic simulations and a simple analytical model yield insight into the underlying mechanisms.

The ground-state magnetization of a thin, soft FM disk is a vortex state with topological charge, or vorticity $q = 1$ in which an in-plane magnetization circulates around a central core [16,17]. At the core, the magnetization is forced out of plane creating a strong, local, dipolelike magnetic fringe field \mathbf{B}_v . The vortex state is characterized by the circulation direction, or chirality $c = \pm 1$ of the vortex (either clockwise or counterclockwise), and the core polarization $p = \pm 1$, indicating the direction $p\hat{z}$ of the out-of-plane magnetization. The behavior of FM vortices in static and time-varying magnetic fields has been previously studied both experimentally and theoretically [18–24]. For a small applied magnetic field \mathbf{B} , the energy of the vortex state with the core displaced by \mathbf{r} from the disk center can be approximated via an effective potential $U(\mathbf{r}, \mathbf{B}) = \frac{1}{2}k|\mathbf{r}|^2 + ck\chi_0(xB_y - yB_x)$, with both the stiffness k and displacement susceptibility χ_0 depending on the disk geometry and material parameters [23]. In equilibrium, the vortex core resides at the minimum of this potential. A static in-plane magnetic field therefore allows control of the vortex core position $\mathbf{r}_v = c\chi_0(-B_y\hat{x} + B_x\hat{y})$. In a time-varying magnetic field, the vortex core undergoes driven motion through the potential U . The nonzero topological charge of the vortex gives rise to a gyrovector $\mathbf{G} = -qpG\hat{\mathbf{z}}$ (G is a constant depending on disk geometry and material parameters), and the resulting dynamics are given by Thiele's equation of

*jab298@case.edu

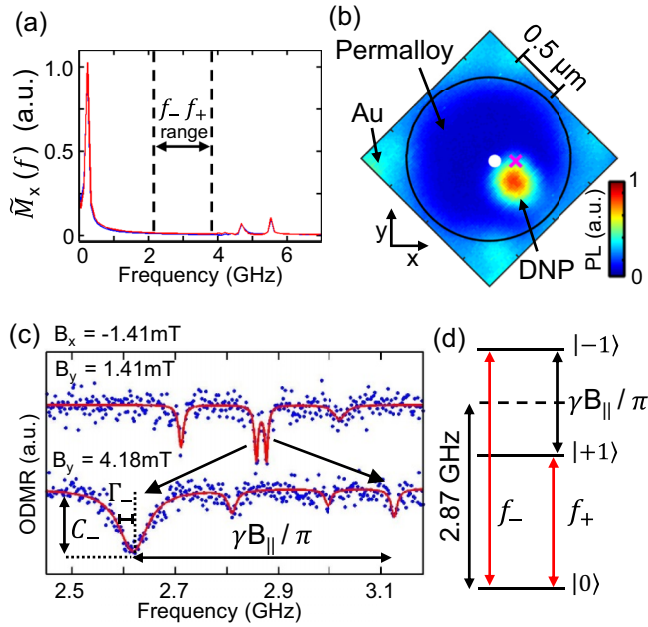


FIG. 1. (a) Simulated frequency spectrum, $\tilde{M}_x(f)$ following perturbation of a 2- μm -diameter, 40-nm-thick disk. The range of NV spin transition frequencies f_+ and f_- is indicated. (b) PL scan of a DNP (red spot) containing several NVs atop a 2- μm -diameter Permalloy disk. (c) ODMR line scans measured at two applied fields, corresponding to vortex core positions shown in (b) (\circ : top, \times : bottom). Lorentzian fits (red line) are plotted over the data with ODMR contrast C_- and transition linewidth Γ_- indicated for the resonance at f_- . With magnetic field projection B_{\parallel} along the NV axis, spin transitions are split by $\gamma B_{\parallel}/\pi$ where $\gamma/(2\pi) = 28 \text{ MHz mT}^{-1}$. (d) Energy level diagram of the relevant NV spin states $m_s = 0, \pm 1$.

motion (EOM) [23]: $\mathbf{G} \times \dot{\mathbf{r}} - \nabla U(\mathbf{r}, \mathbf{B}) = 0$ (neglecting the small vortex mass [24] and damping terms for simplicity).

The dynamics of the vortex result in a spectrum of modes, which depend on the geometry of the disk. Figure 1(a) shows the simulated [25] spectrum $\tilde{M}_x(f)$, of the x component of magnetization averaged over a 2- μm -diameter, 40-nm-thick disk, following a step in magnetic field from $B_x = 1\text{--}0 \text{ mT}$. The dominant feature near 200 MHz corresponds to gyrotropic precession [18] of the vortex core about its equilibrium position at frequency $\omega_0 = k/G$, as described by the EOM above. The smaller features at $f > 4 \text{ GHz}$ arise from confined spin-wave modes [19]. Of interest here is the frequency range $f = 2.5\text{--}3.3 \text{ GHz}$, which is well into the dispersive regime, away from any resonances. To describe how the vortex dynamics couple to proximal NV spins, we will focus on dispersive coupling to the gyrotropic mode, though the higher-frequency spin wave modes may also play a role.

In a driving field $\mathbf{b}e^{i\omega t}$, the vortex core EOM has solutions of the form $\mathbf{r}(t) = \boldsymbol{\rho}e^{i\omega t}$ [20], where $\boldsymbol{\rho}$ is determined by the Polder tensor:

$$\boldsymbol{\rho} = \begin{pmatrix} -i\rho_1 & \rho_0 & 0 \\ \rho_0 & i\rho_1 & 0 \\ 0 & 0 & 0 \end{pmatrix} \begin{pmatrix} b_x \\ b_y \\ b_z \end{pmatrix}. \quad (1)$$

In the regime of interest here ($\omega \gg \omega_0$), $\rho_0 \approx c\chi_0(\omega_0/\omega)^2$, and $\rho_1 \approx pc\chi_0(\omega_0/\omega)$.

The driven motion of the vortex core results in a time-varying magnetic fringe field $\mathbf{b}_v(\mathbf{x})e^{i\omega t}$ above the disk. Assuming the motion of the vortex core is small compared to the spatial scale of \mathbf{B}_v , then $\mathbf{b}_v \approx \nabla \mathbf{B}_v \cdot \boldsymbol{\rho}$, where the gradient tensor $\nabla \mathbf{B}_v$ generally has all nine elements nonzero. As a result, the total microwave field $\mathbf{b}_{\text{ac}} = \mathbf{b} + \mathbf{b}_v$ generally has all three components complex and nonzero.

The effect of the vortex on the NVs arises as the vortex fringe field contributes to the total magnetic field $\mathbf{B}_{\text{tot}} = \mathbf{B} + \mathbf{B}_v(\mathbf{x}) + \mathbf{b}_v(\mathbf{x})e^{i\omega t}$ entering into the Zeeman term in the NV spin Hamiltonian: $H = hDS_z^2 + \hbar\gamma(\mathbf{B}_{\text{tot}}) \cdot \mathbf{S}$. Here, h is Planck's constant, $D = 2.87 \text{ GHz}$ is the zero-field splitting along the NV axis denoted z' , $\gamma/(2\pi) = 28 \text{ MHz/mT}$, and \mathbf{S} is the vector of spin-one Pauli matrices. The time-independent components of the total field \mathbf{B}_{tot} shift the frequencies of the $|m_s = 0\rangle$ to $|m_s = \pm 1\rangle$ transitions, while the time-dependent component \mathbf{b}_{ac} can resonantly drive these transitions.

Transitions from the $|0\rangle$ to $|\pm 1\rangle$ spin states of the NV ground state proceed at a rate given by the Rabi frequency $\Omega_{\pm} = \gamma|(\pm 1|\mathbf{b}_{\text{ac}} \cdot \mathbf{S}|0)|$ when ω is resonant with one of the transitions. In a circularly polarized basis about the NV axis \hat{z}' , the Rabi frequencies reduce to $\Omega_+ = \gamma|b_-|$ and $\Omega_- = \gamma|b_+|$, where $b_{\pm} = (b_{x'} \pm ib_{y'})/2$. For a driving field with no phase difference between $b_{x'}$ and $b_{y'}$, $\Omega_+ = \Omega_-$, as is the case for the linearly polarized applied MW field. However, the chiral nature of the vortex dynamics gives rise to a general phase shift between the components of \mathbf{b}_v when $\rho_1 \neq 0$ in Eq. (1). The NV/vortex coupling thereby results in $\Omega_+ \neq \Omega_-$.

NVs are placed in proximity to a FM vortex by overcoating 2- μm -diameter, 40-nm-thick Permalloy disks with NV-containing diamond nanoparticles (DNPs). The disks are fabricated atop a Au coplanar waveguide (CPW) for application of static and MW magnetic fields. The DNPs have a mean diameter of 25 nm and contain zero to several NV defects. A photoluminescence (PL) scan of the specific vortex/DNP studied is shown in Fig. 1(b). The black circle indicates the edge of the disk, with a DNP that contains several NVs appearing as the bright red spot in the bottom right quadrant of the disk.

Measurements are carried out on a scanning confocal microscopy setup at room temperature that combines an optically detected magnetic resonance (ODMR) technique [5] for NV spin-state control and readout and a differential magneto-optical Kerr effect (MOKE) technique for tracking the vortex position [26]. The position of the vortex core is controlled by a magnetic field supplied by permanent magnets and dc current through the CPW. MOKE measurements provide values $c = 1$ and $\chi_0 = 80 \text{ nm/mT}$, yielding a calibration of vortex displacement vs applied field. MW current through the CPW also supplies the ac driving field. See Ref. [8] for further details on the samples and techniques.

To illustrate the effect of moving the vortex core closer to the NVs, Fig. 1(c) shows two ODMR scans with the vortex core at positions indicated in Fig. 1(b). Both scans reveal two pairs of transitions, from NVs in two different orientations. Each pair of transitions is characterized by the center frequencies f_+ and f_- , contrast C_+ and C_- , and half width at half maximum Γ_+ and Γ_- [see Fig. 1(d)]. Henceforth we will focus on the pair of transitions from the NV orientation with greater C_+ and C_- . The energy difference between the $|+1\rangle$ and $|-1\rangle$ states is

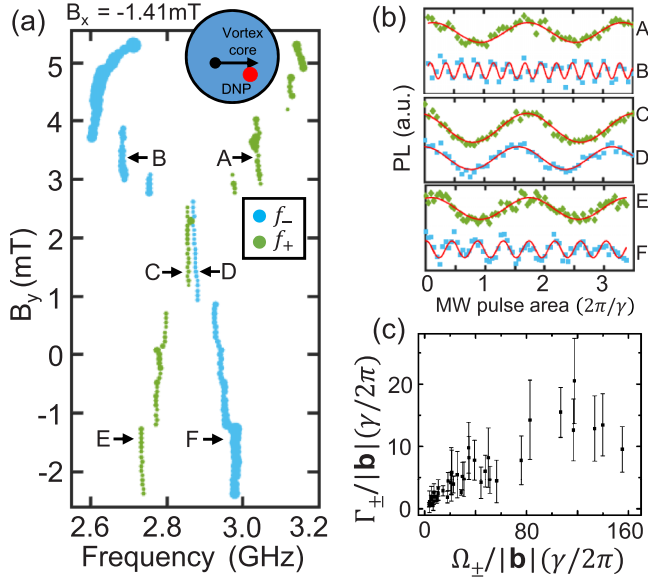


FIG. 2. (a) Transition frequencies f_+ and f_- as the vortex is translated along the path in the inset by sweeping B_y at a static B_x . The size of each point indicates Γ . (b) Rabi oscillations vs MW pulse area (product of pulse duration and MW field amplitude $|\mathbf{b}|$) measured at the points A–F indicated in (a), with fits to a sinusoidal function (red). (c) $\Gamma/|\mathbf{b}|$ vs $\Omega/|\mathbf{b}|$ in units of $\gamma/(2\pi)$, at different in-plane magnetic fields. Error bars for Ω are small relative to the error in Γ and are not shown.

revealed by the splitting of f_+ and f_- about D by $(\gamma/\pi)\mathbf{B}_{\text{tot}} \cdot \hat{z}'$. To extract the parameters describing the resonances, we fit the scans to multiple Lorentzians (red line). The differences between the two scans are largely caused by the influence of the static and dynamic fringe field \mathbf{B}_v and \mathbf{b}_v , which are both larger in the bottom scan when the vortex core is closer to the NVs. Here, \mathbf{B}_v is the main cause of the spin splitting (the applied field alone can account for at most 20% of the observed splitting) and \mathbf{b}_v is the cause of the enlarged Γ_+ and Γ_- . The latter relationship is the result of the vortex dynamics affecting the NV spin dynamics and is the focus of this paper.

We now probe the evolution of the vortex/NV coupling while translating the vortex along a path near the NVs. Figure 2(a) plots f_+ and f_- with Γ_+ and Γ_- indicated by the size of the points as the vortex is driven by sweeping B_y with a static B_x . The resulting path of the vortex core is illustrated in the inset. As expected, the largest splitting between f_+ and f_- occurs when the vortex core approaches the NVs at $B_y \approx 4$ mT. Further, Γ_+ and Γ_- both attain their largest values when the vortex core is near the NVs, with typically $\Gamma_+ < \Gamma_-$.

To understand how the vortex affects Γ_+ and Γ_- , we measure Ω_+ and Ω_- directly by driving Rabi oscillations with MW pulses of amplitude $|\mathbf{b}|$ and duration t_p at the selected points A–F in Fig. 2(a). The resulting oscillations between $|0\rangle$ and $|\pm 1\rangle$ vs MW pulse area $|\mathbf{b}|t_p$, plotted in Fig. 2(b) in units of $2\pi/\gamma$, are fit to a sinusoidal function to obtain Ω_+ or Ω_- . In the absence of vortex/NV interactions, one would expect a Rabi period $\geq 4\pi/\gamma$. From this data, we can see that some transitions have significantly enhanced Ω , and that this enhancement is correlated to enhanced Γ . This correlation

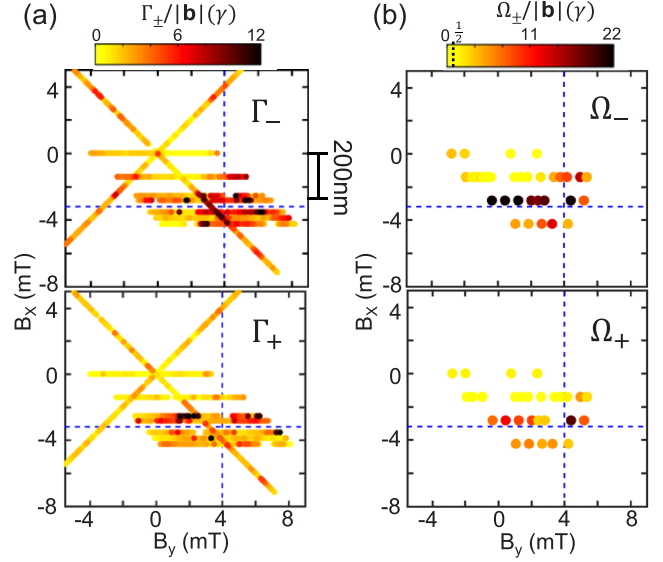


FIG. 3. (a) A spatial map of $\Gamma_{\pm}/|\mathbf{b}|$ (top) and $\Gamma_{\pm}/|\mathbf{b}|$ (bottom) measured at different applied B_x and B_y . The vortex core is closest to the NVs roughly at the intersection of the blue dashed lines. The scale bar indicates the vortex core translation with applied field. (b) $\Omega_{\pm}/|\mathbf{b}|$ (top) and $\Omega_{\pm}/|\mathbf{b}|$ (bottom) measured at selected applied B_x and B_y .

suggests that measurements of Γ provide a relaxometric probe of Ω . Although Rabi oscillations are a more direct measure of Ω , a relaxometry technique provides a more efficient method for mapping out the NV/vortex interactions. To confirm the correspondence between the Rabi and relaxometry methods, values of Γ and Ω from a range of vortex positions across the disk are plotted in Fig. 2(c) revealing a roughly linear relationship. Furthermore, we have previously observed a linear relationship between Γ and $|\mathbf{b}|$ [8], which allows us to choose a sufficiently strong $|\mathbf{b}|$ to ensure that the dominant source of broadening is from the driving of the vortex, and not incoherent thermal motion of the vortex.

By repeating the vortex core line scan shown in Fig. 2(a) at different static fields, we can construct a spatial map of the influence of the dynamic vortex. Figure 3(a) shows values of Γ_+ and Γ_- vs in-plane applied field, where the vortex core is swept along two long diagonal paths, and seven shorter horizontal paths near the NVs. The value of Γ_+ and Γ_- at each applied field point is extracted from the fit to the resonance at f_+ and f_- . At selected applied field values with the vortex core near the NVs, we measure Ω_+ or Ω_- directly via Rabi oscillations at f_+ or f_- [Fig. 3(b)], providing a more precise confirmation of the relaxometry measurement. Given the measured value of χ_0 , the applied field can be converted into vortex core position, indicated by the scale bar. The maps show that Ω_+ and Ω_- are enhanced by more than an order a magnitude as the vortex core approaches the NVs, located approximately at the dashed cross (with no enhancement, the maximum value of $\Omega/|\mathbf{b}| = \gamma/2$). Alternatively, the data in Fig. 3(b) can be interpreted as a map of the two orthogonal components b_+ and b_- of the fringe field perpendicular to the NV axis, and resonant with the driving field. The region of strong enhancement has a radius of approximately 200 nm

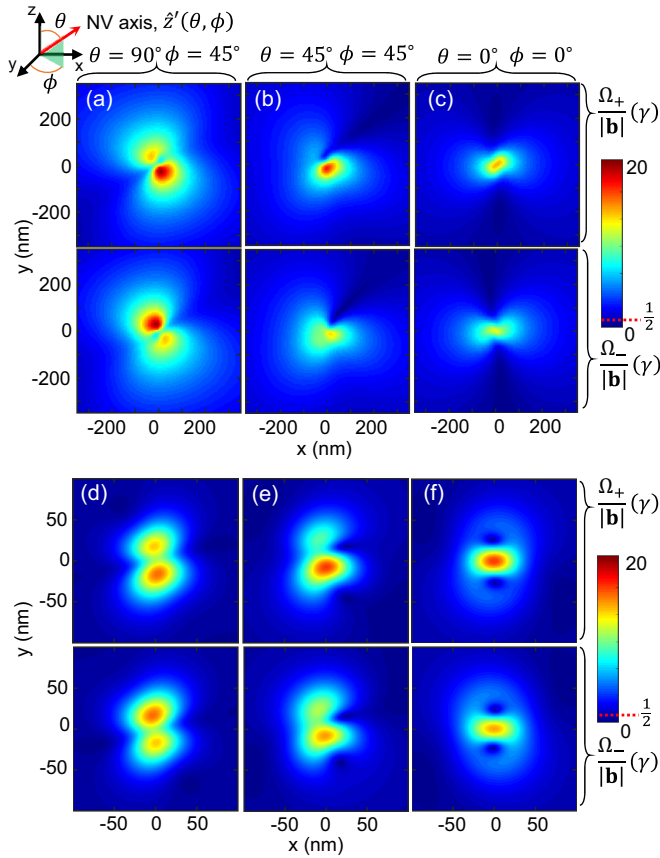


FIG. 4. (a)–(c) Micromagnetic simulation of \mathbf{b}_{ac} , yielding Ω_+ and Ω_- for an NV with orientation $\hat{z}'(\theta, \phi)$. The images show a $(700 \text{ nm})^2$ range at the center of the disk. (d)–(f) Analytical calculation of Ω_+ and Ω_- for the same orientations in (a)–(c). Note the smaller $(200 \text{ nm})^2$ range.

centered near the NV position. The chiral nature of the vortex dynamics is imprinted on the spin transitions resulting in $\Omega_+ \neq \Omega_-$. The trend of $\Omega_- > \Omega_+$ seen in the line scan in Fig. 2 is generally borne out in the maps in Fig. 3, particularly in the region of large enhancement.

Micromagnetic simulations capture a general understanding of the chiral nature of the vortex dynamics. We obtain \mathbf{b}_{ac} in a plane $\approx 30 \text{ nm}$ above a $2\text{-}\mu\text{m}$ -diameter, 40-nm -thick disk, in response to a driving field $b_x = 0.05 \text{ mT}$ at $f = 2.8 \text{ GHz}$. The simulated \mathbf{b}_{ac} is projected onto a plane normal to $\hat{z}'(\theta, \phi)$,

and resolved into circularly polarized components b_+ and b_- , yielding simulated values for Ω_+ and Ω_- (see Supplemental Material [27] for more details). Figures 4(a)–4(c) show $\Omega_+/|\mathbf{b}|$ and $\Omega_-/|\mathbf{b}|$ for three different \hat{z}' . In general, these simulation results reproduce the measured magnitude and the spatial scale of the enhancement. The differences between Ω_+ and Ω_- indicate the elliptical polarization of \mathbf{b}_{ac} . Though all \hat{z}' show areas of elliptical polarization, the relative orientation of \hat{z}' and the gyrovector \mathbf{G} sets whether the chirality produces an overall preferred polarization. With $\hat{z}' \perp \mathbf{G}$ in Fig. 4(a), there are equal regions of enhancement of Ω_+ and Ω_- . In contrast, with $\hat{z}' \parallel \mathbf{G}$ in Fig. 4(c), there is an overall enhancement of Ω_+ over Ω_- . The simulations also show asymmetry in the spatial dependence of Ω_+ and Ω_- when \hat{z}' is not parallel to \mathbf{G} , with the largest effect occurring away from the vortex core position. This asymmetry also seems to be present in the data in Fig. 3. The intermediate case in Fig. 4(b) is likely most representative of the measured \hat{z}' in the randomly oriented nanoparticle.

Comparison to an analytical calculation provides insight into the measured and simulated vortex dynamics. We approximate \mathbf{B}_v as the field from a magnetic dipole $\mathbf{d} = d\hat{z}$, with $d = 1.1 \times 10^7 \text{ mT nm}^3$ calculated by integrating M_z over the vortex core [28], and calculate \mathbf{b}_v as described above, using Eq. (1). The resulting values of $\Omega_+/|\mathbf{b}|$ and $\Omega_-/|\mathbf{b}|$ are shown in Figs. 4(d)–4(f) for the same three \hat{z}' . These maps show qualitative agreement with the micromagnetic simulations, suggesting that the effect can be roughly understood as arising from the driven motion of the dipolelike vortex core. However, the spatial scale of the enhancement is significantly smaller than in the simulation and experiment. It is possible that this difference could be explained by also considering the confined spin-wave modes, which have a larger spatial scale than the gyrotropic mode, or by considering a more general dynamic deformation of the magnetization state.

These results show that a ferromagnetic element, beyond providing a static fringe field, can have a strong dynamic influence on a proximal coherent spin. This effect may be controlled by tailoring the magnetization state of the FM, and could lead to applications involving enhancement of magnetic fields for sensing, or interactions between spins mediated by the proximal ferromagnet.

This work was supported by the U.S. Department of Energy, Office of Science, Basic Energy Sciences, under Award No. DE-SC008148.

- [1] Y. Tabuchi, S. Ishino, A. Noguchi, T. Ishikawa, R. Yamazaki, K. Usami, and Y. Nakamura, *Science* **349**, 405 (2015).
- [2] M. Pioro-Ladrière, T. Obata, Y. Tokura, Y.-S. Shin, T. Kubo, K. Yoshida, T. Taniyama, and S. Tarucha, *Nature Phys.* **4**, 776 (2008).
- [3] R. Jansen, *Nature Mater.* **11**, 400 (2012).
- [4] D. A. Simpson, J. P. Tetienne, J. M. McCoe, K. Ganesan, L. T. Hall, S. Petrou, R. E. Scholten, and L. C. L. Hollenberg, *Sci. Rep.* **6**, 22797 (2016).
- [5] R. Schirhagl, K. Chang, M. Loretz, and C. L. Degen, *Annu. Rev. Phys. Chem.* **65**, 83 (2014).
- [6] J. M. Taylor, P. Cappellaro, L. Childress, L. Jiang, D. Budker, P. R. Hemmer, A. Yacoby, R. Walsworth, and M. D. Lukin, *Nature Phys.* **4**, 810 (2008).
- [7] P. Maletinsky, S. Hong, M. S. Grinolds, B. Hausmann, M. D. Lukin, R. L. Walsworth, M. Loncar, and A. Yacoby, *Nature Nanotechnol.* **7**, 320 (2012).
- [8] M. S. Wolf, R. Badea, and J. Berezovsky, *Nature Commun.* **7**, 11584 (2016).

- [9] L. Rondin, J.-P. Tetienne, S. Rohart, A. Thiaville, T. Hingant, P. Spinicelli, J. F. Roch, and V. Jacques, *Nature Commun.* **4**, 2279 (2013).
- [10] J.-P. Tetienne, T. Hingant, L. Rondin, S. Rohart, A. Thiaville, J.-F. Roch, and V. Jacques, *Phys. Rev. B* **88**, 214408 (2013).
- [11] T. van der Sar, F. Casola, R. Walsworth, and A. Yacoby, *Nature Commun.* **6**, 7886 (2015).
- [12] M. Schaffry, E. M. Gauger, J. J. L. Morton, and S. C. Benjamin, *Phys. Rev. Lett.* **107**, 207210 (2011).
- [13] L. Trifunovic, F. L. Pedrocchi, S. Hoffman, P. Maletinsky, A. Yacoby, and D. Loss, *Nature Nanotechnol.* **10**, 541 (2015).
- [14] C. S. Wolfe, V. P. Bhallamudi, H. L. Wang, C. H. Du, S. Manuilov, R. M. Teeling-Smith, A. J. Berger, R. Adur, F. Y. Yang, and P. C. Hammel, *Phys. Rev. B* **89**, 180406 (2014).
- [15] R. Badea, M. S. Wolf, and J. Berezovsky, *Appl. Phys. Lett.* **109**, 132403 (2016).
- [16] T. Shinjo, T. Okuno, R. Hassdorf, K. Shigeto, and T. Ono, *Science* **289**, 930 (2000).
- [17] A. Wachowiak, J. Wiebe, M. Bode, O. Pietzsch, M. Morgenstern, and R. Wiesendanger, *Science* **298**, 577 (2002).
- [18] J. P. Park and P. A. Crowell, *Phys. Rev. Lett.* **95**, 167201 (2005).
- [19] T. Y. Chen, A. T. Galkiewicz, and P. A. Crowell, *Phys. Rev. B* **85**, 180406 (2012).
- [20] K. Yu. Guslienko, *Appl. Phys. Lett.* **89**, 022510 (2006).
- [21] K. Yu. Guslienko, V. Novosad, Y. Otani, H. Shima, and K. Fukamichi, *Appl. Phys. Lett.* **78**, 3848 (2001).
- [22] G. Wysin, *Phys. Rev. B* **54**, 15156 (1996).
- [23] K. Yu. Guslienko, B. A. Ivanov, V. Novosad, Y. Otani, H. Shima, and K. Fukamichi, *J. Appl. Phys.* **91**, 8037 (2002).
- [24] K. Yu. Guslienko, X. F. Han, D. J. Keavney, R. Divan, and S. D. Bader, *Phys. Rev. Lett.* **96**, 067205 (2006).
- [25] M. J. Donahue and D. G. Porter. OOMMF User's Guide, Version 1.0, Interagency Report NISTIR 6376, National Institute of Standards and Technology, Gaithersburg, Maryland, 1999. The code is available at <http://math.nist.gov/oommf>.
- [26] R. Badea, J. A. Frey, and J. Berezovsky, *J. Magn. Magn. Mater.* **381**, 463 (2015).
- [27] See Supplemental Material at <http://link.aps.org/supplemental/10.1103/PhysRevB.96.014424> for details on the simulations and analytical model.
- [28] R. Hollinger, A. Killinger, and U. Krey, *J. Magn. Magn. Mater.* **261**, 178 (2003).